Article

Research on the Performance Characteristics and Unsteady Flow Mechanism of a Centrifugal Pump under Pitch Motion

Ye Yuan [1,2,*], **Weihong Gong** [3], **Guojun Wang** [4] **and Jun Wang** [1]

1   School of Energy and Power, Jiangsu University of Science and Technology, Zhenjiang 212100, China
2   Wenling Institute of Fluid Machinery, Jiangsu University, Wenling 317523, China
3   Harbin Marine Boiler & Turbine Research Institute, Harbin 150078, China
4   Wenling Institute of Product Quality Inspection, Wenling 317599, China
*   Correspondence: yuanye@just.edu.cn

Abstract: Pitch motion is the key factor affecting the performance characteristics of centrifugal pumps on board ships and exacerbates hydraulic excitation to induce the unsteady vibration of pump units. A hydraulic test platform with swing motion is established to explore the effects of pitch motion on a pump's performance characteristics. An obvious hump zone exists in the head characteristic curve in the low-flow-rate condition due to the pitch motion. The pump head in the shut-off condition has a significant decrease due to the pitch motion, compared to the static state. The head decrease gradually increases as the maximum pitch angle increases or the pitch period shortens. Specifically, the head in the rated flow condition decreases by 6.3 % to reach a minimum at the maximum pitch angle of 20 degrees in a period of 5 s. Based on a multiple-reference coordinate system, a large eddy simulation with a shear-modified eddy viscosity model is employed to simulate inner flow characteristics under the influence of pitch motion. A distinct vortex flow appears near the blade suction surface and becomes increasingly turbulent as the pitch period shortens. The pitch motion intensifies the unsteady stretching and deformation of vortices. The periodic variations in fluid-induced pressure over time present parabolic features, and the amplitude in the frequency domain reaches its maximum value within a pitch period of 5 s.

Keywords: centrifugal pump; pitch motion; performance characteristics; unsteady flow; vortex dynamic

1. Introduction

Ship pumps are key pieces of equipment in ship machinery. Centrifugal pumps account for over 80% of ship pumps and are used for ship ballast balance, pipeline heat exchange circulation, ship safety, fire protection, domestic water supply and drainage systems. The pumps on board ships are affected by the ocean environment, causing pitch motion, and their inner flow is subjected to additional swing forces, resulting in more turbulent flow and more intense flow excitation which induce the unsteady vibration of pump systems [1–3].

Under the influence of pitch motion, the flow rate inside a pipeline undergoes pulsating variation, and the average flow rate is lower than that in the static state. The flow rate undergoes periodic fluctuations under the influence of pitch motion, and the fluctuation period is consistent with the pitch period [4,5]. Simultaneously, the fluctuation amplitude is enhanced with increases in pitch frequency and amplitude. When the pitch motion is severe, there may even be backflow in the loop pipeline [6–8]. The pitch motion can also cause adjacent parallel pipelines to oscillate in the same direction, but the symmetrical arrangement and arrangement structure of pipelines can reduce the effects of the pitch. Low-speed pitch motion has a relatively small impact on the frictional pressure drop of pipeline flow but increases the effect of the Coriolis inertial force to result in significant variations in the flow structure. As the Coriolis inertial force increases, some unsteady flows,

such as secondary vortex flows, appear in circular pipes [9–11]. This unsteady flow occurs in the inlet pipes of pumps and then forms a non-uniform flow structure before impeller inlets, which affects the performance and inner flow characteristics of pumps [12–14].

Specifically, the performance characteristics of a centrifugal pump undergo significant variations in the tilt state and under the influence of pitch motion. The pump head has an experimental descending amplitude, and some significant flow-induced fluctuations are present in the pressure development [15–17]. Under the influence of pitch motion, there is a significant peak–valley phenomenon in the pressure fluctuation inside the pump. As the swinging angle increases, the amplitude of flow-induced pressure fluctuation gradually increases, and the maximum increase reaches 15%. When the centrifugal pump is tilted, the average amplitude of pressure fluctuation increases by 15% for the blade-passing frequency and 18% for the shaft frequency [18–20]. The influence of pitch motion and the tilt state reduce the performance characteristics of the pump and exacerbate flow-induced vibration features.

Pitch motion can cause pulsating variations in the flow rate and can induce a secondary vortex structure to affect flow stability. This paper focuses on the effects of pitch motion on the performance characteristics and unsteady flow mechanism of a centrifugal pump. A hydraulic test platform with swing motion is established to test the pump's performance. A large eddy simulation with a shear-modified eddy viscosity model is employed to analyze the unsteady characteristics in flow development. This work provides some evidence analyzing the effects of pitch motion on the operation characteristics of centrifugal pumps, aiming to have important engineering significance and academic value in the design and manufacturing of high-tech ships.

2. Materials and Methods

2.1. Centrifugal Pump Model

A single-stage centrifugal pump with a spiral volute was selected as the study object in this work. The pump's rated flow rate was selected as 15 m³/h and the head as 16 m. The impeller rotation speed was set at 2900 r/min. The impeller's three-dimensional shape was parameterized using fourth-order Bezier curves for the hub, shroud and blade characteristics. The volute with a circular cross section was designed using the Stepanoff method, ensuring a consistent absolute velocity along the circumferential direction under the rated operation conditions. Detailed geometric information on the model pump is listed in Table 1.

Table 1. Design requirement of centrifugal pump.

impeller inlet diameter/m	0.04
impeller outlet diameter/m	0.16
blade outlet width/m	0.006
blade number	5
blade wrap angle/°	120
blade inlet angle/°	22
blade outlet angle/°	24
volute base circle diameter/m	0.162
volute outlet diameter/m	0.032

2.2. Experimental Devices and Methods

In order to explore the variations in the performance characteristics of the centrifugal pump in an ocean environment, a hydraulic test platform with swing motion for the pump was established. The experiment set was composed of the model pump, an ocean wave simulation platform with six degrees of freedom, flexible pipes used for pump inlet and outlet connections, a surge tank, electric butterfly valves and other water pipelines (see Figure 1). The tested data were acquired and collected by a centrifugal pump performance test system with a torque speed sensor, pressure sensor and electromagnetic flowmeter. The surge tank provided circulating water which entered the pump suction

pipe through an electric butterfly valve. Pressure sensors were mounted in the inlet and outlet pipelines, arranged at a distance twice the diameter of the pipe away from the pump inlet or outlet. The ring pressure chamber was used to gain steady pressures of pump inlet and outlet pipelines. The flow rate data were obtained by an electromagnetic flowmeter mounted in the pump outlet pipeline. The upstream and downstream pipeline lengths of the flowmeter were more than 10 times longer than the pipe diameter.
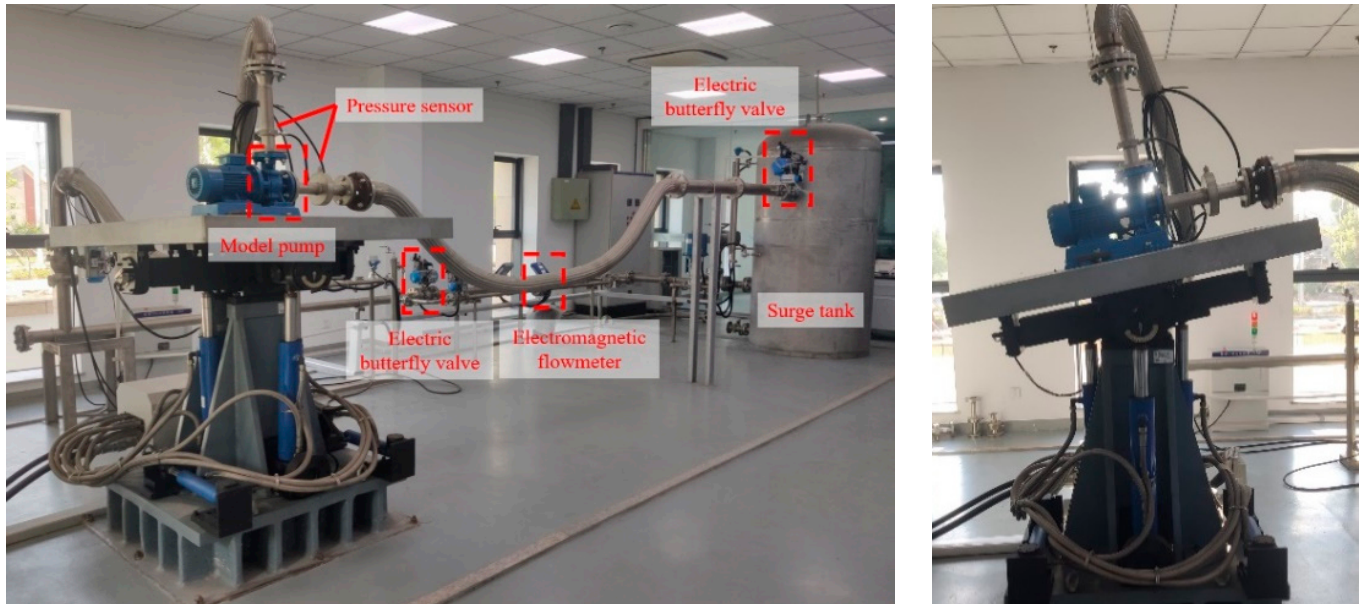

Figure 1. Centrifugal pump swing test platform.

To understand the performance characteristics of the model pump, the head coefficient (ψ), hydraulic efficiency (η) and flow rate coefficient (φ) were selected to compare pump performances under the static state and pitch motion and were defined as follows:

$$\psi = \frac{P_{out}^T - P_{in}^T}{\frac{1}{2}\rho U_2^2} \tag{1}$$

$$\eta = \frac{(P_{out}^T - P_{in}^T)Q}{T\omega} \tag{2}$$

$$\varphi = \frac{Q}{2\pi\omega R_2^2 B_2} \tag{3}$$

where P^T, ρ, U_2, Q, T, ω, R_2 and B_2 are the total pressure, water density, blade tip velocity, pump flow rate, torque, impeller angular velocity, impeller diameter and impeller outlet width, respectively. The subscripts 2, in and out indicate the impeller outlet and measuring locations at the pump inlet and pump outlet, respectively.

Tested performance characteristics of the model pump under the static state are displayed in Figure 2. The maximum efficiency occurs at the rated flow condition (φ_d). Meanwhile, ψ presents a steadily sloping curve across the φ/φ_d range, and the maximum ψ appears at the shut-off condition. The ψ curve and the η curve indicate that the model pump has good hydraulic performance.
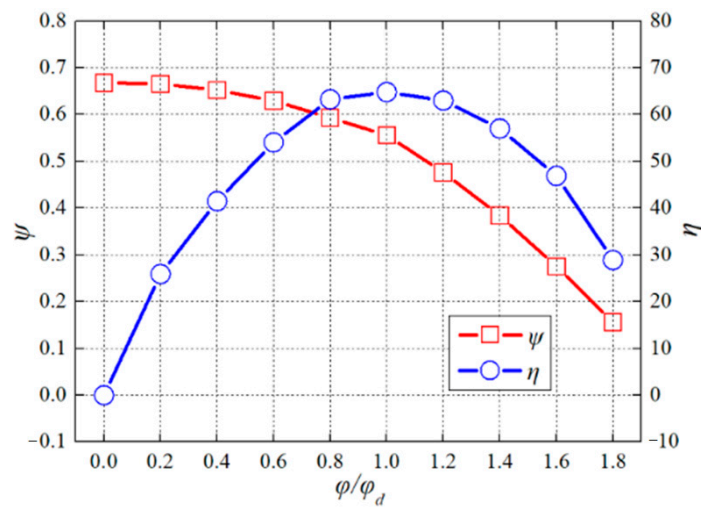
Figure 2. Pump performance characteristics under static state.

2.3. CFD Methodology

Numerical simulations were applied to determine the inner flow characteristics of the model pump under the influence of pitch motion. The computational domain of the model pump is exhibited in Figure 3, including the impeller passage, volute chamber and extensions of the inlet and outlet. A hexahedral mesh was implemented on each independent domain as shown in Figure 3. The maximum nondimensional wall distance y+ value of the computational domain was chosen to be less than 1. The grid independence was analyzed by the grid convergence index (GCI) defined in Equation (4) [21], as shown in Table 2. Considering the computing capacity and grid error, a mesh with 1.2×10^7 grid points was adopted on account of the ψ values at the pump's rated flow rate.

$$\mathrm{GCI}_k = \varepsilon_s \frac{r^i_{k,k+1} \varphi_{r(k,k+1)}}{r^i_{k,k+1} - 1} \tag{4}$$

where ε_s is the safety factor and takes value from 1.25 to 3.00, $r^i_{k,k+1}$ is the mesh refinement ratio and $\varphi_{r(k,k+1)}$ is the relative error between grids.
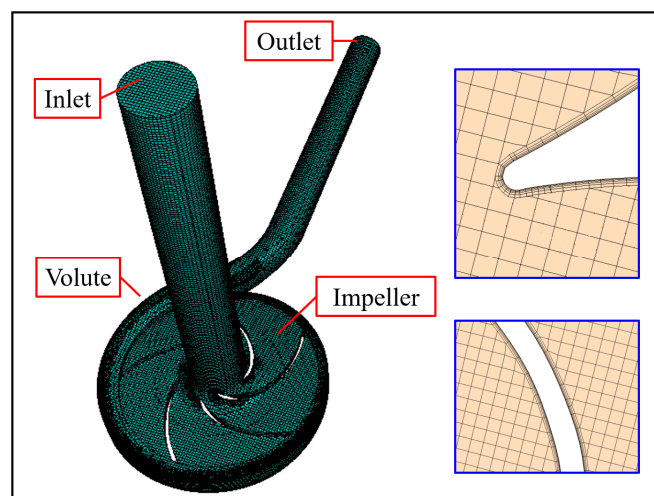

Figure 3. Computation domain and grid system.

A large eddy model was employed to simulate the inner flow characteristics of the model pump proposed in this work. Equations (5) and (6) were processed from the Navier–Stokes equations and the continuity equation under the instantaneous state by

the filter function. The Smagorinsky model was optimized to solve the problems in the vortex motion on the basis of Equations (7)–(10). A shear-modified eddy viscosity model considering the strong shear near the wall was applied in the large eddy simulation. The optimized eddy viscosity model met the requirements of vortex motion simulation near the wall's surface [22]. The original eddy viscosity coefficient μ_τ^0 was changed to the new eddy viscosity coefficient μ_τ in Equations (9) and (10).

$$\frac{\partial}{\partial t}\left(\rho \bar{u}_i\right)+\frac{\partial}{\partial x_j}\left(\rho \bar{u}_i \bar{u}_j\right) = -\frac{\partial \bar{p}}{\partial x_i} + \frac{\partial}{\partial x_j}\left(\mu \frac{\partial \bar{u}_i}{\partial x_j}\right) - \frac{\partial \tau_{ij}}{\partial x_j} \tag{5}$$

$$\frac{\partial \rho}{\partial t} + \frac{\partial}{\partial x_i}\left(\rho \bar{u}_i\right) = 0 \tag{6}$$

$$\tau_{ij} = \rho \overline{u_i u_i} - \rho \bar{u}_i \bar{u}_j \tag{7}$$

$$\tau_{ij} - \frac{1}{3}\tau_{kk}\delta_{ij} = -2\mu_\tau^0 \bar{K}_{ij} \tag{8}$$

$$\mu_\tau^0 = (c_s \Delta)^2 \left|\bar{K}\right| \tag{9}$$

where $\bar{K}_{ij} = \frac{1}{2}\left(\frac{\partial \bar{u}_i}{\partial x_j} + \frac{\partial \bar{u}_j}{\partial x_i}\right)$, $\left|\bar{K}\right| = \sqrt{2\bar{S}_{ij}\bar{S}_{ij}}$, $\Delta = (\Delta_x \Delta_y \Delta_z)^{\frac{1}{3}}$ and Δ_i represents the network size along the i axis.

$$\mu_\tau = (c_v \Delta)^2 \left(\left|\bar{K}\right| - \left|f\langle \bar{K}\rangle\right|\right) \tag{10}$$

where $f = 1 - (1 - c_0)^{\frac{\text{th}[c_1(y^+ - y_0^+)]+1}{2}}$, $c_v = 0.02$, $c_0 = 0.05$, $y_0^+ = 50$ and $c_1 = 32$.

Table 2. Analysis of grid convergence for different numbers of elements.

Parameters		Values
Number of elements	$N_1/N_2/N_3$	$9.4 \times 10^6 / 1.2 \times 10^7 / 2.1 \times 10^7$
Computed head coefficients (ψ) corresponding to N_1, N_2 and N_3	$\psi_1/\psi_2/\psi_3$	0.565/0.561/0.559
Apparent order	p	1.32
Grid convergence index corresponding to N_1, N_2 and N_3	$GCI_1/GCI_2/GCI_3$	3.08%/2.12%/1.93%

Based on the pisoFoam solver of the OpenFOAM 4.0 platform, a multiple-reference coordinate system was used to achieve the simulation of pitch motion. The pitch coordinate system was constructed as the pitch foundation for the entire computational domain of the model pump. The inlet boundary was set to "velocity" with an accurate velocity component on the basis of pump operation conditions. The outlet boundary condition was set to "outlet" with reference to experiment data. Figure 4 reveals the simulated performance characteristics compared with tested data under the static state and the influence of pitch motion with a maximum pitch angle of 20 degrees and a pitch period of 5 s. The simulated ψ and η were less than 2.5% and 3.5% of tested results at the rated flow rate, respectively, which illustrated that the simulated results were in good agreement with tested data. The simulated results were a little higher than the tested data, which was due to hydraulic loss and mechanical loss in the pump. The hydraulic loss concentrated on leakage losses in the static chamber between the pump casing and the impeller, while the mechanical loss covered the dynamic imbalance of the impeller and the machining error of the pump's critical component such as the impeller and the drive shaft.
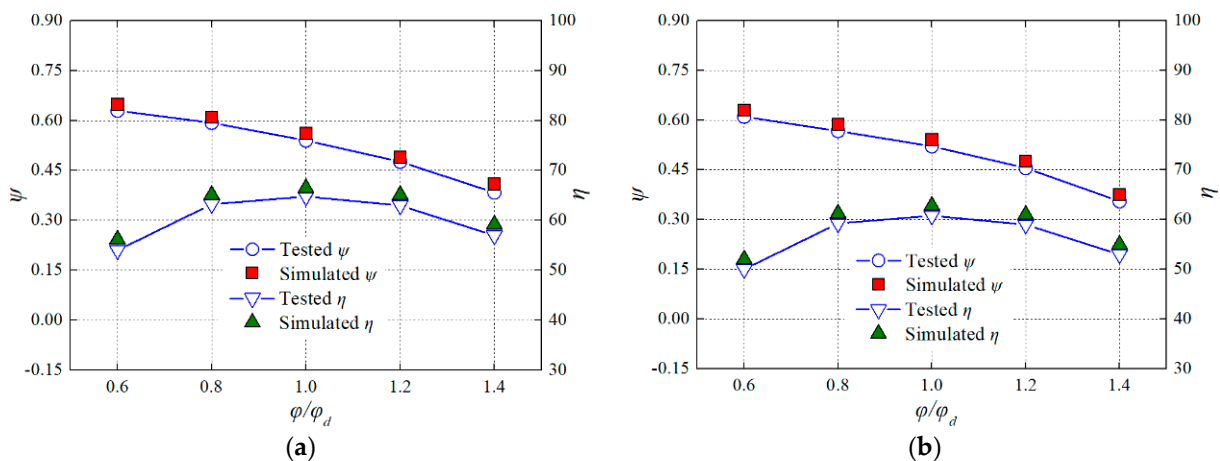
Figure 4. Comparison between simulated and tested performance characteristics: (**a**) static, (**b**) pitch motion.

3. Result and Discussion

3.1. Pump Test Performances under Pitch Conditions

The pitch direction of the tested pump is along the upward or downward pitch direction of the pump's inlet pipe, exhibited in Figure 5. The transient pitch angle is defined as $\theta(x)$ in Equation (11).
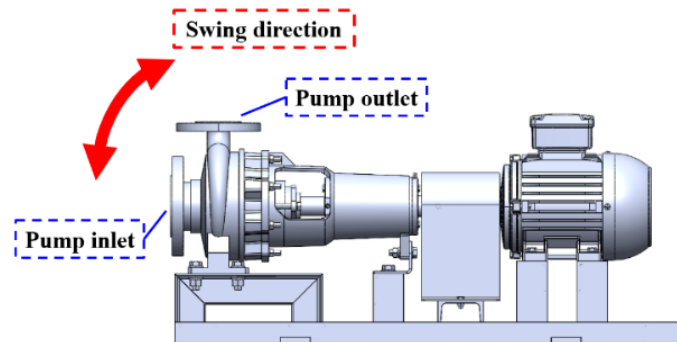

Figure 5. Centrifugal pump pitch direction.

Based on the actual pitch conditions of a pump system on board a ship in a marine environment and relevant standards of International Association of Classification Societies, pitch motion parameters are determined as shown in Table 3, including maximum pitch angle and pitch period. The maximum pitch angle covers four levels and the pitch period covers three levels in the pitch experiment scheme of the tested pump.

$$\theta(x) = \theta_{max} \sin \frac{2\pi x}{k} \tag{11}$$

where θ_{max} is the maximum pitch angle and k is the pitch period.

Table 3. Pitch experiment scheme.

	Level 1	Level 2	Level 3	Level 4
θ_{max}/degree	5	10	15	20
k/second	5	10	20	

Figure 6 compares the performance curves for the static state and across different levels of pitch motion with three periods of 5 s, 10 s and 20 s under a maximum pitch angle

of 5 degrees. Figure 6a shows an obvious hump zone present in these curves under the influence of pitch motion for $\varphi/\varphi_d \leq 0.4$, which causes unstable operating characteristics such as a sudden drop in pump outlet pressure or severe pump vibration and noise. The hump curve induces two flow-rate points under the same water pressure condition, which generates pulsating variations in pump flow rate and then produces some instability flows and flow excitation. Specifically, ψ experiences a small reduction at $\varphi/\varphi_d = 0$ under the influence of pitch motion and decreases as the pitch period shortens. When model pump is in a static state, ψ reaches a maximum at $\varphi/\varphi_d = 0$. However, the occurrence of maximum ψ shifts to a higher value of φ/φ_d ($\varphi/\varphi_d = 0.2$). Figure 6 indicates that the performance curves for ψ represent similar slopes at $\varphi/\varphi_d \geq 0.6$, where ψ decreases as the pitch period reduces. The ψ curves for pitch motion conditions of 10 degrees, 15 degrees and 20 degrees show variations quite similar to those under pitch motion conditions of 5 degrees across the whole φ/φ_d range, as shown in Figures 7–9. Unsteady variation characteristics of pump performance including the hump curve and ψ reduction become more and more obvious as the pitch angle increases.
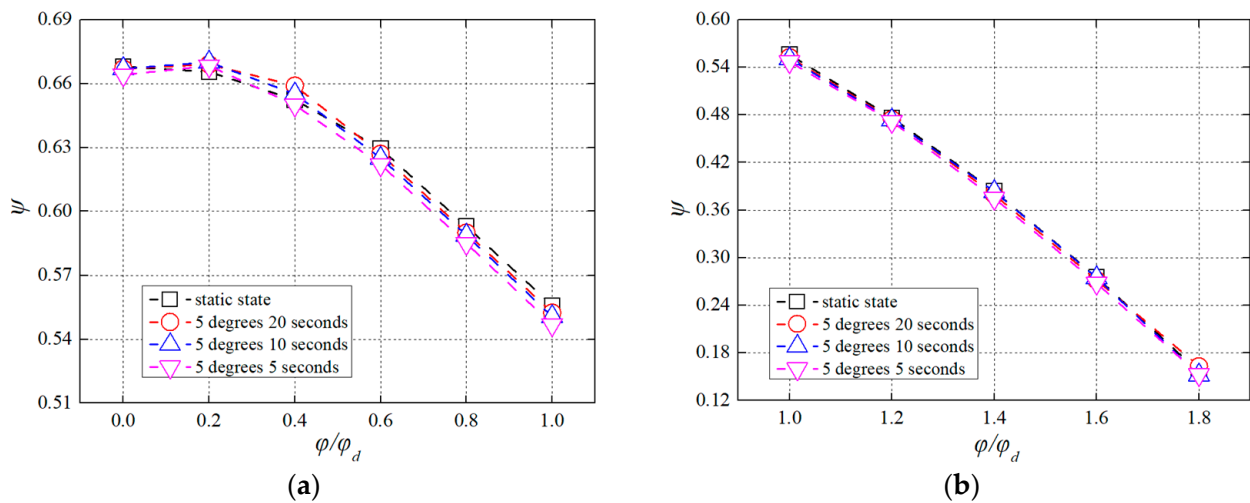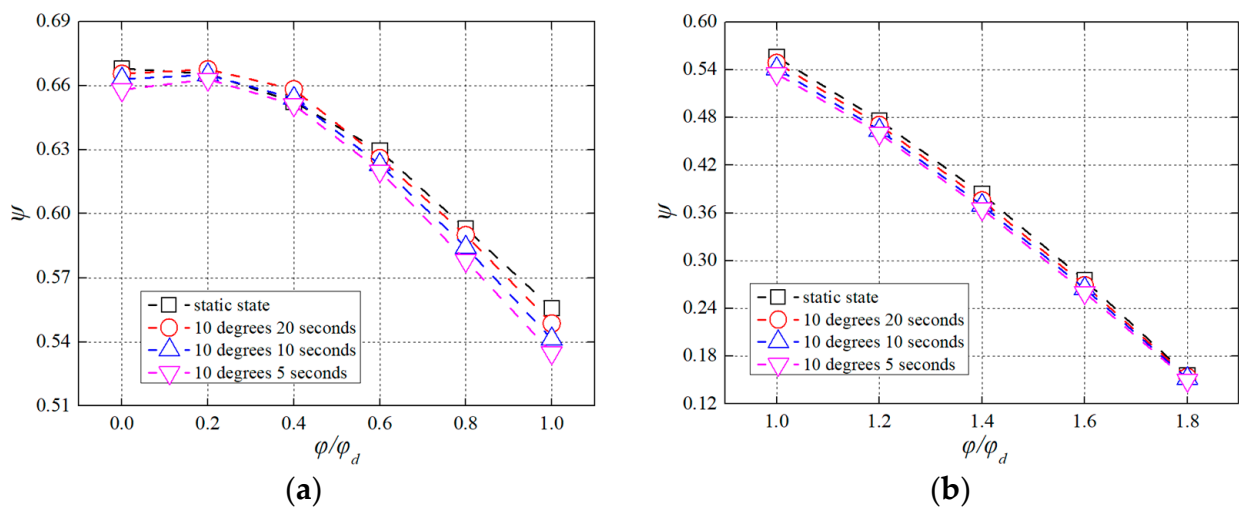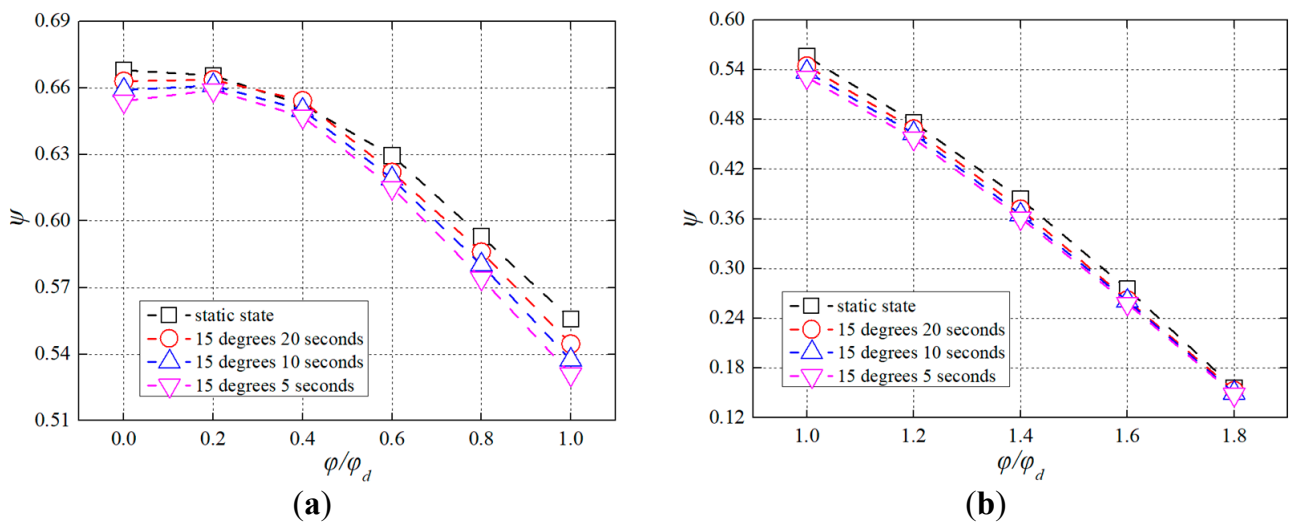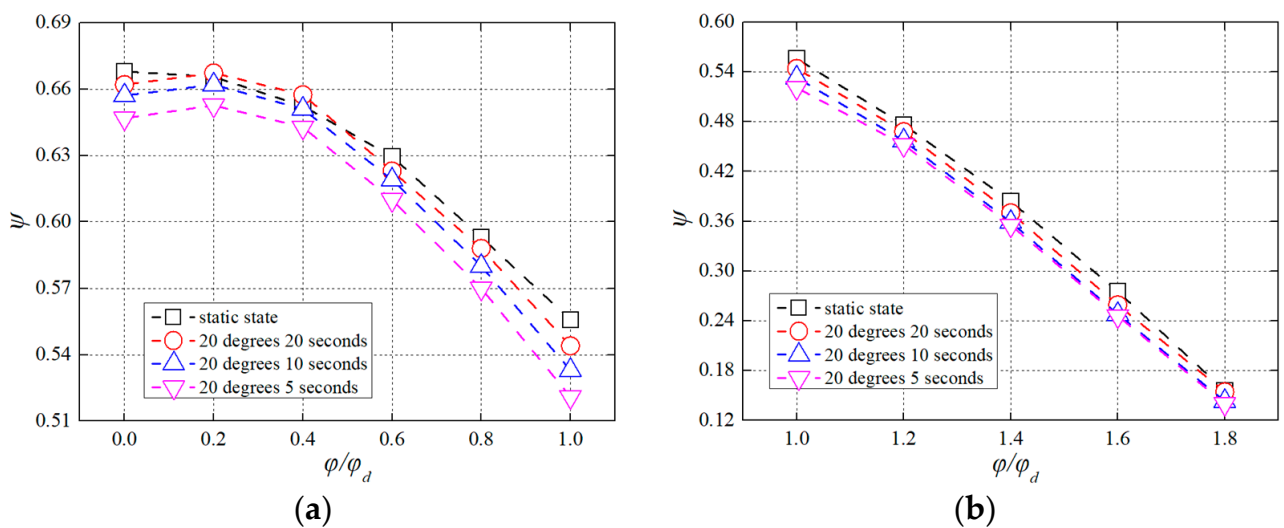

Figure 6. Comparison of performance curves for static state and different levels of pitch motion with three periods of 5 s, 10 s and 20 s under the maximum pitch angle of 5 degrees: (**a**) $\varphi/\varphi_d \leq 1.0$, (**b**) $\varphi/\varphi_d \geq 1.0$.

Figure 7. Comparison of performance curves for static state and different levels of pitch motion with three periods of 5 s, 10 s and 20 s under the maximum pitch angle of 10 degrees: (**a**) $\varphi/\varphi_d \leq 1.0$, (**b**) $\varphi/\varphi_d \geq 1.0$.

Figure 8. Comparison of performance curves for static state and different levels of pitch motion with three periods of 5 s, 10 s and 20 s under the maximum pitch angle of 15 degrees: (**a**) $\varphi/\varphi_d \leq 1.0$, (**b**) $\varphi/\varphi_d \geq 1.0$.

Figure 9. Comparison of performance curves for static state and different levels of pitch motion with three periods of 5 s, 10 s and 20 s under the maximum pitch angle of 20 degrees: (**a**) $\varphi/\varphi_d \leq 1.0$, (**b**) $\varphi/\varphi_d \geq 1.0$.

Furthermore, pump performance curves for the static state and different levels of pitch motion with maximum pitch angles of 5 degrees, 10 degrees, 15 degrees and 20 degrees for a pitch period of 20 s are compared in Figure 10. ψ maintains an evident reduction across the φ/φ_d range as the maximum pitch angle increases. The ψ difference becomes more obvious as the pitch period shortens according to Figures 11 and 12. Particularly, the ψ difference reaches a maximum at a pitch period of 5 s. Under the pump operating condition of φ_d shown in Figure 13, the pitch motion causes a significant decrease in ψ compared to the static state. ψ reduces as the maximum pitch angle increases for the same pitch period. Meanwhile, ψ reduces as the pitch period shortens for the same pitch angle. ψ decreases by 6.3% to reach a minimum at a maximum pitch angle of 20 degrees and a pitch period of 5 s.
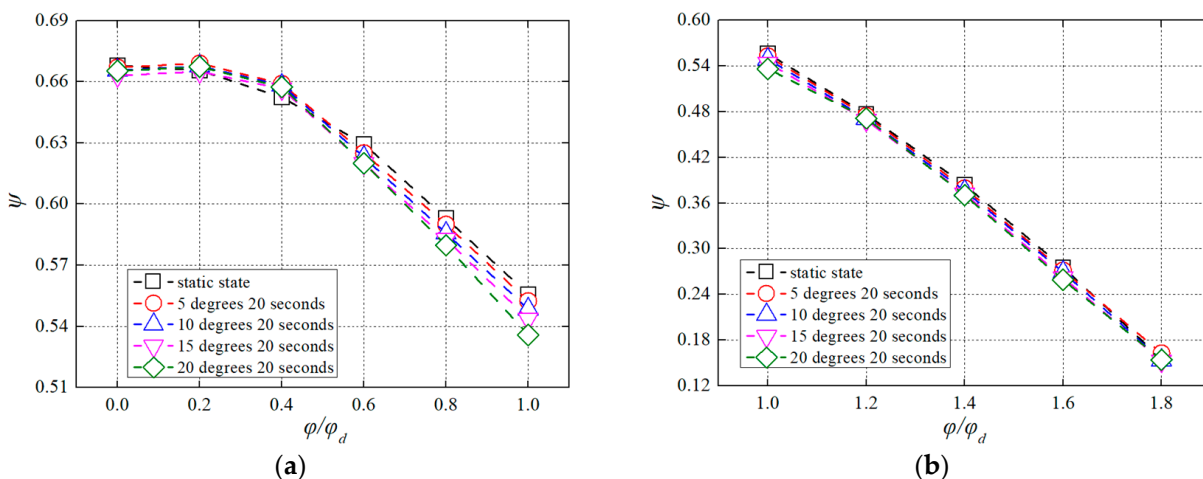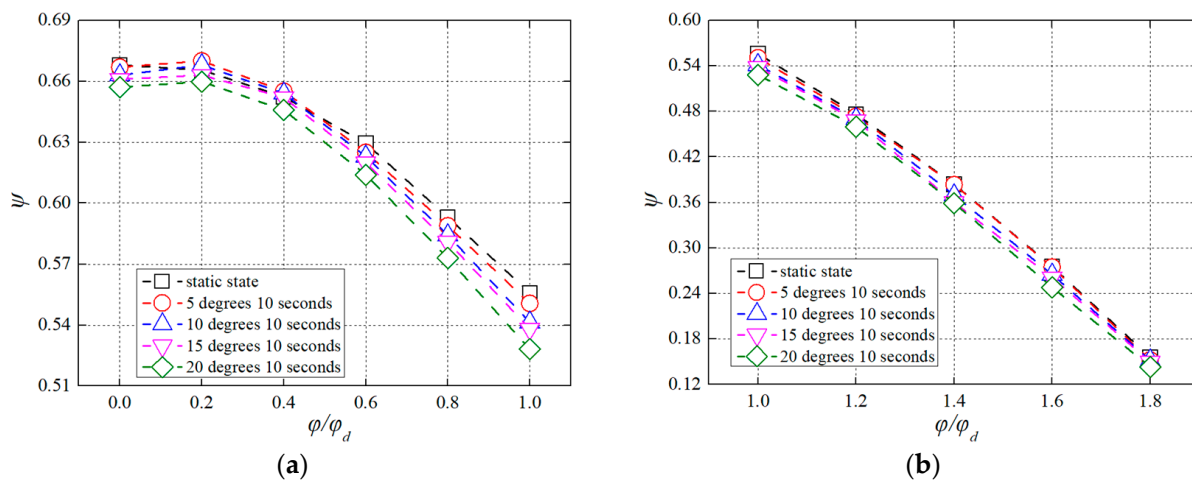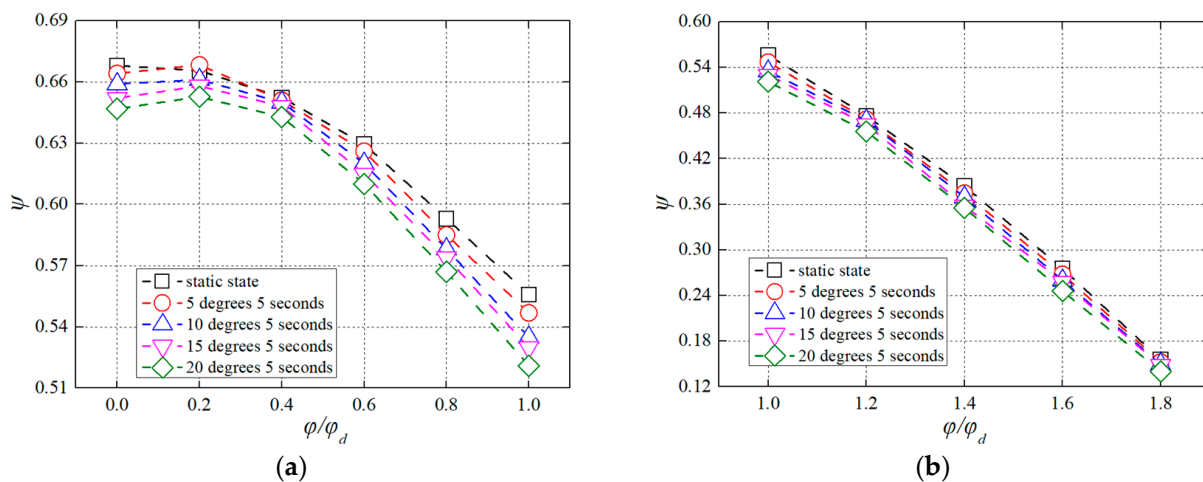
Figure 10. Comparison of performance curves for static state and different levels of pitch motion with maximum pitch angles of 5 degrees, 10 degrees, 15 degrees and 20 degrees for a pitch period of 20 s: (**a**) $\varphi/\varphi_d \leq 1.0$, (**b**) $\varphi/\varphi_d \geq 1.0$.

Figure 11. Comparison of performance curves for static state and different levels of pitch motion with maximum pitch angles of 5 degrees, 10 degrees, 15 degrees and 20 degrees for a pitch period of 10 s: (**a**) $\varphi/\varphi_d \leq 1.0$, (**b**) $\varphi/\varphi_d \geq 1.0$.
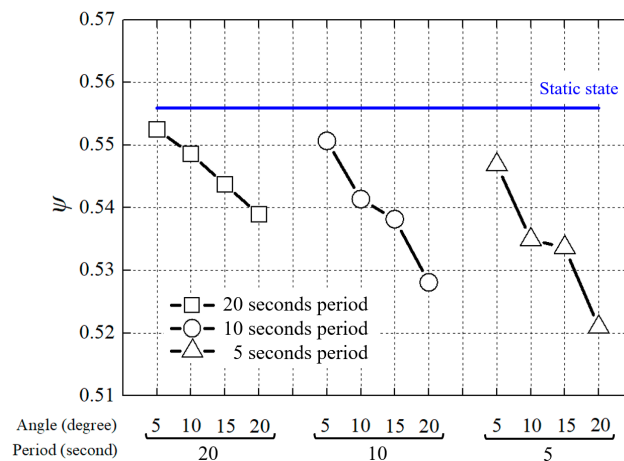

Figure 12. Comparison of performance curves for static state and different levels of pitch motion with maximum pitch angles of 5 degrees, 10 degrees, 15 degrees and 20 degrees for a pitch period of 5 s: (**a**) $\varphi/\varphi_d \leq 1.0$, (**b**) $\varphi/\varphi_d \geq 1.0$.

Figure 13. The ψ variation under pitch motion at φ_d.

3.2. Flow Characteristics under Pitch Motion

Pump performance characteristics have a more significant decrease for a pitch angle of 20 degrees, compared to other pitch angles. Thus, the flow structure under conditions of a 20-degree pitch angle is used to investigate the effect of pitch motion on inner flow characteristics. Figures 14 and 15 show the velocity distributions to characterize the flow structure in the single-blade inlet and single-blade outlet during the model pump's operation from static state to pitch motion respectively. The flow velocity near the blade presents a rapid increase, primarily influenced by the viscous force of the fluid. A slope velocity distribution exists in the main passage under the static state. Nevertheless, the velocity curve under pitch motion maintains a negative slope, where the velocity decreases as the pitch period shortens. Compared with static state, the velocity gradient increases in the blade passage inlet under pitch motion, while the velocity gradient remains constant in the blade passage outlet. This means that the pitch motion mostly affects the flow structure in the blade inlet, not in the blade outlet. The flow characteristics in the blade outlet are affected by the combined action of the rotating impeller and pitch motion.
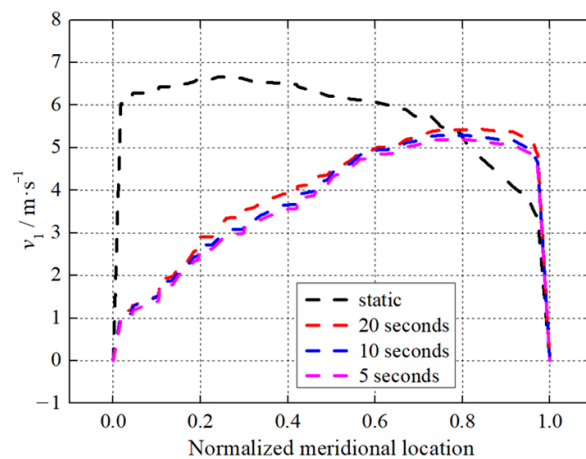

Figure 14. Velocity distributions along the normalized meridional locations for blade passage inlet.

The blade pressure surface (convex surface) is applied convert blade mechanical energy into water energy, while the blade suction surface (concave surface) has low-velocity regions produced by some stall flows under the influence of pitch motion, as shown in Figure 16. The area of the low-velocity region gradually increases as the pitch period shortens, and the stall flow becomes increasingly turbulent. The flow is highly unsettled near the blade suction surface, which may be due to the existence of the vortex core in the blade passage shown in Figure 17. The wrapping of the low-velocity region by some

high-velocity fluids in the form of layers may broadly represent a core structure. Uneven flow distribution appears in the blade passage and high tangential flow velocity relates to local flow separation, which contributes to the unsteady pitch motion.
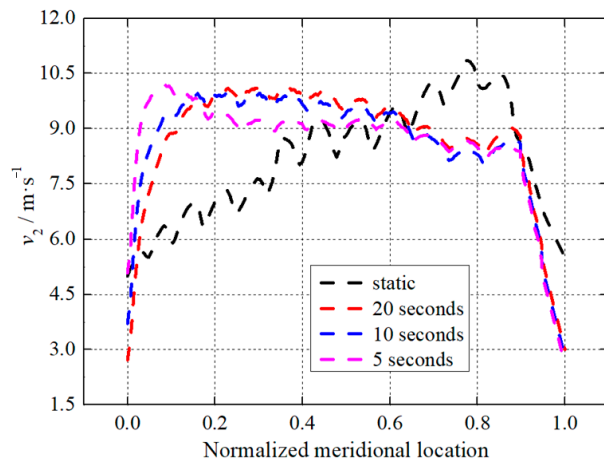

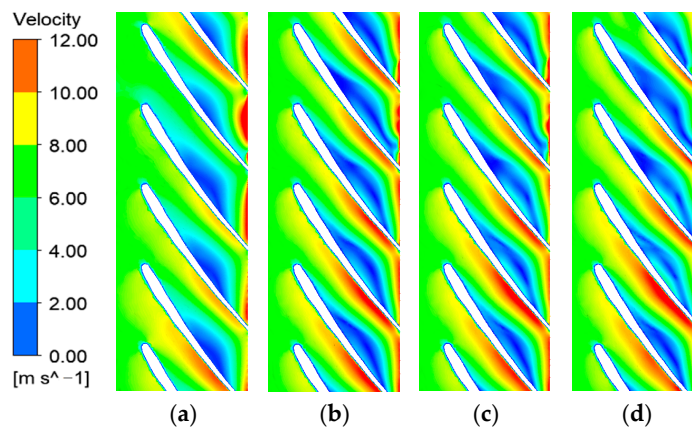**Figure 15.** Velocity distributions along the normalized meridional locations for blade passage outlet.

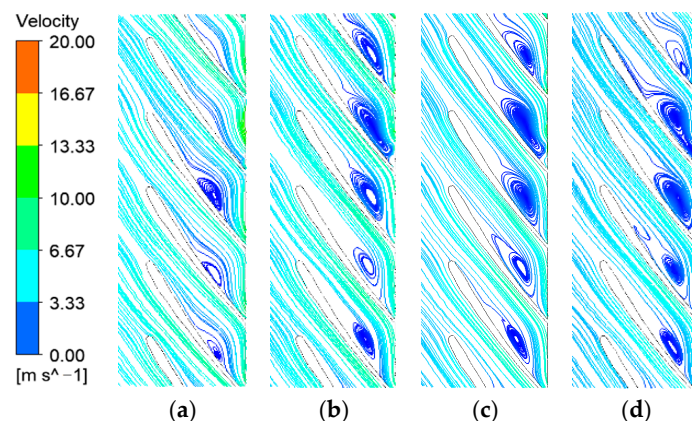**Figure 16.** Flow structures under different pitch motion periods: (**a**) static, (**b**) 20 s, (**c**) 10 s, (**d**) 5 s.

Figure 17. Unsteady flows under different pitch motion periods: (**a**) static, (**b**) 20 s, (**c**) 10 s, (**d**) 5 s.

The pitch environment causes intense unsteady vortex motion in the blade passage, which may be the main reason for the decrease in pump performance. The relative vorticity transport equation [23–25] is introduced to analyze the inception, evolution and dissipation

of blade passage vortex motion to obtain a profound understanding of the flow mechanism. The equation in the relative coordinate system is given in Equation (12).

$$\frac{D\vec{Q}_r}{Dt} = (\vec{Q}_r \cdot \nabla)\vec{W} - \vec{Q}_r(\nabla \cdot \vec{W}) - 2\nabla \times (\omega._r \times \vec{W}) + \frac{\nabla\rho \times \nabla P}{\nabla\rho^2} + \nu\nabla^2\vec{Q}_r \quad (12)$$

where $\vec{Q}_r$ denotes the relative vorticity, $\vec{W}$ denotes the relative velocity, ω_r denotes the rotation angular velocity and ν denotes the kinematic viscosity.

The left item of $\frac{D\vec{Q}_r}{Dt}$ in Equation (12) represents the variation rate of vorticity. The rightmost item of $(\vec{Q}_r \cdot \nabla)\vec{W}$ represents the relative vortex stretching (RVS) related to the relative velocity gradient. $\vec{Q}_r(\nabla \cdot \vec{W})$ represents the relative vortex dilation (RVD) related to relative velocity divergences. $.2\nabla \times (\omega._r \times \vec{W})$ is the effect of the Coriolis force (CORF) related to the rotational motion. $\frac{\nabla\rho \times \nabla P}{\nabla\rho^2}$ is attributed to the baroclinic torque. $\nu\nabla^2\vec{Q}_r$ is the viscous diffusion item (VISD) due to fluid viscosity. $\vec{Q}_r(\nabla \cdot \vec{W})$ and $\frac{\nabla\rho \times \nabla P}{\nabla\rho^2}$ are ignored due to fluid incompressibility.

The RVS term indicates the effect of the fluid velocity gradient on the generation of vorticity. The fluid velocity evolves along the vortex line, which results in the stretching, twisting and tilting of the vorticity. The velocity gradient parallel to the vortex line causes the stretching of vorticity, while the velocity gradient perpendicular to the vortex line brings about the distortion of vorticity. The deformation and stretching of vortices weaken the moment of inertia of the fluid element, which increases the angular velocity to generate vorticity. Figure 18 shows the distributions of RVS in the impeller passage under different pitch periods. The big velocity gradient leads to the stretching or twisting of vortex lines in the flow passage. The unsteady behaviors of vortices are mainly concentrated in the inlet area of the impeller. The pitch environment induces severe vortex motion, which intensifies as the pitch period shortens.
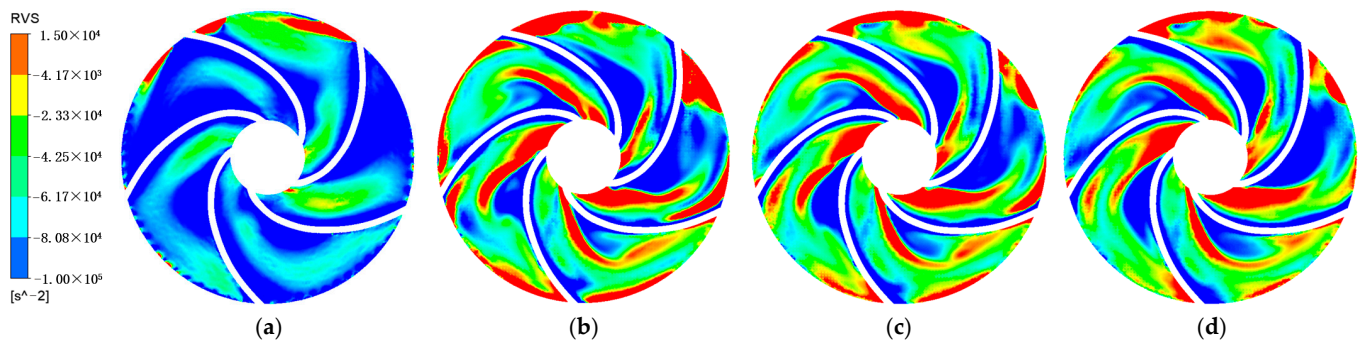

Figure 18. RVS distributions under different pitch periods: (**a**) static, (**b**) 20 s, (**c**) 10 s, (**d**) 5 s.

The Coriolis force term is an inertial force generated by the movement of fluid particles relative to the coordinate system, which leads to the motion deviation of the particle in the rotating flow field. The Coriolis force acts perpendicular to the direction of motion of fluid particles and, thus, only changes the motion direction and not the flow velocity. The characteristics of the Coriolis force vary according to the pitch motion. Figure 19 shows the distributions of CORF in the impeller passage under different pitch periods. Distinctly, the pitch environment induces intense vortex motion, mainly occurring near the blade suction surface and the impeller outlet. As the pitch period shortens, the vortex motion becomes more pronounced due to the Coriolis force term. The VISD term represents the conversion of mechanical energy into thermal energy caused by viscous friction. VISD distributions mainly occur in the blade suction surface due to the effects of viscous forces in the velocity

boundary layer, as shown in Figure 20. This phenomenon has been strengthened by pitch motion.
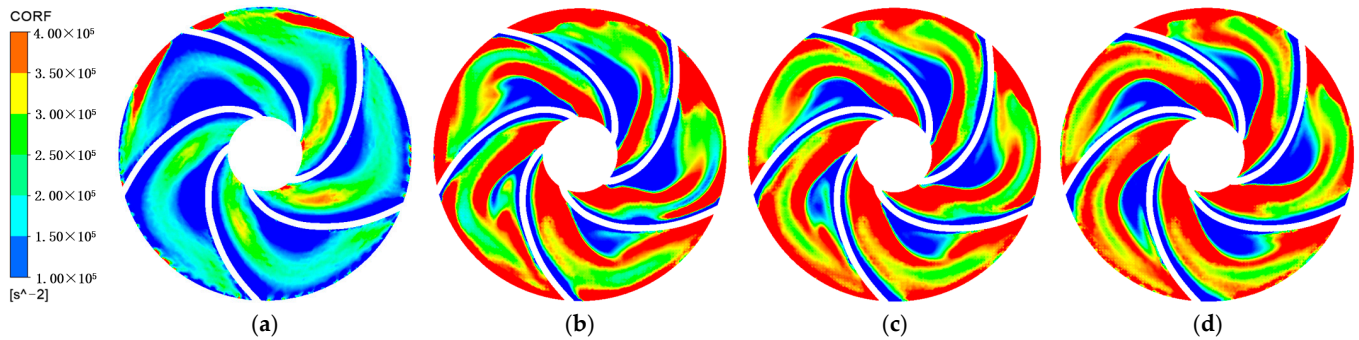

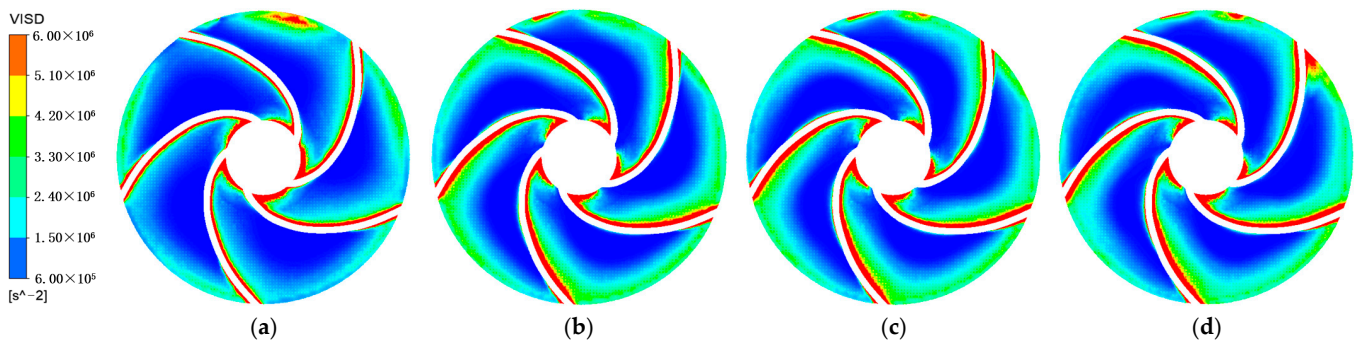**Figure 19.** CORF distributions under different pitch periods: (**a**) static, (**b**) 20 s, (**c**) 10 s, (**d**) 5 s.

Figure 20. VISD distributions under different pitch periods: (**a**) static, (**b**) 20 s, (**c**) 10 s, (**d**) 5 s.

3.3. Unsteady Pressure Characteristics

The influence of pitch motion intensifies the unsteady flow of fluid inside the pump, inducing unsteady pressure excitation. The static pressure coefficient (C_P) is employed to evaluate the pressure distribution map in the pump.

$$C_P = \frac{P_{out}^T - P}{\frac{1}{2}\rho U_2^2} \tag{13}$$

where P^T, P, ρ and U_2 are the total pressure, static pressure, water density and blade tip velocity, respectively. The subscripts 2 and out indicate the impeller outlet and the measuring location at the pump outlet, respectively.

The pressure distribution at the blade inlet is relatively uniform, and C_P curves have similar slopes under the static state and under the influence of pitch motion, exhibited in Figure 21. The pressure magnitude gradually decreases as the pitch period shortens. Nevertheless, C_P curves exhibit opposite slopes at the blade outlet between the static state and under the influence of pitch motion as shown in Figure 22. The pitch motion provides an additional force and varies the force characteristics and motion behaviors of fluid particles. The shape of the blade determines the law of pressure variation. Under the static state, the pressure development rate gradually increases along the blade passage and reaches a maximum at the outlet as shown in Figure 23a. Specially, the maximum pressure increase occurs in the middle section of the blade passage under the influence of pitch motion and the area with low pressure increase gradually increases; this phenomenon is most obvious under the minimum pitch period of 5 s as shown in Figure 23. The pressure gradient map indicates that the pitch motion makes the unsteady flow inside the impeller passage more turbulent.
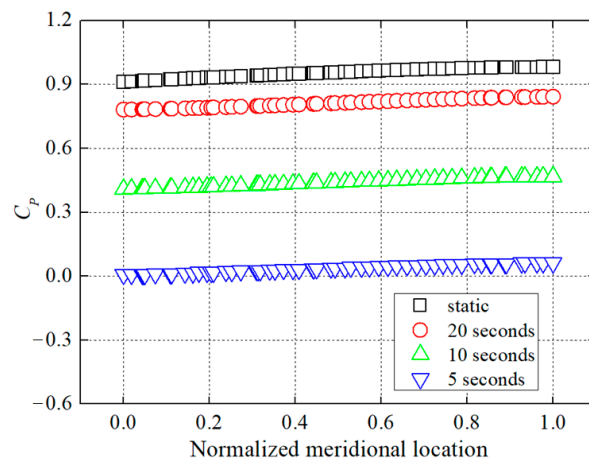
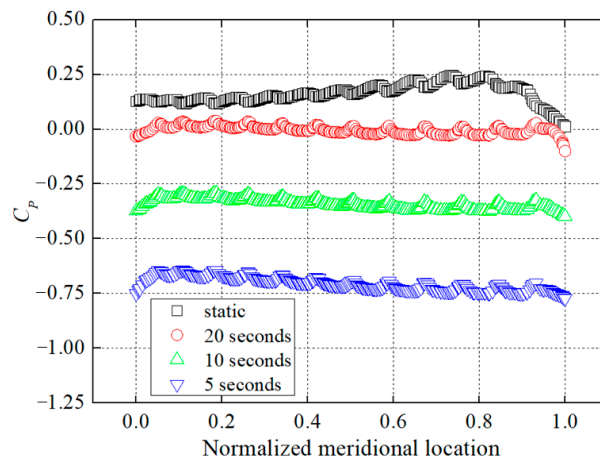**Figure 21.** Pressure distributions along the normalized meridional locations for blade passage inlet.

Figure 22. Pressure distributions along the normalized meridional locations for blade passage outlet.
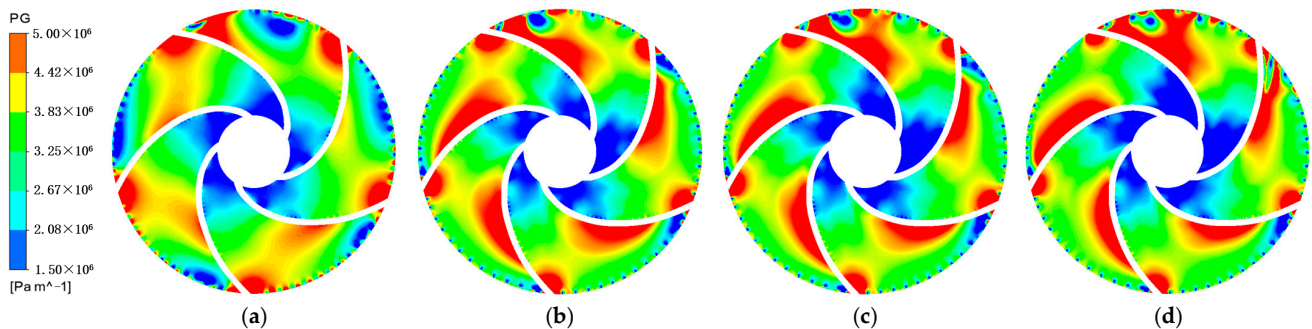

Figure 23. Pressure gradients under different pitch periods: (**a**) static, (**b**) 20 s, (**c**) 10 s, (**d**) 5 s.

Pressure excitation variations with time at the impeller inlet and outlet are monitored to explore the effects of pitch motion on unsteady flow. The pressure variations in one impeller rotation period are recorded in Figures 24 and 25 under the static state and the influence of pitch motion. Five distinct peaks appear in the pressure variation under the static state, corresponding to the blade number. The pressure curves demonstrate that the time-domain variation in pressure mainly depends on the blade characteristics [26–28]. A parabolic feature is present in the pressure curve under the influence of pitch motion, and the parabola's amplitude gradually increases as the pitch period shortens. This phenomenon indicates that the faster the pitching motion, the more excited the unsteady flow in the pump. Figures 26 and 27 present a frequency analysis of pressure variations for the impeller inlet and outlet under the static state and the influence

of pitch motion. The amplitude of pressure pulsation occurs at the shaft frequency and the blade-passing frequency. The pitch motion increases some low-frequency pulsations occurring between 10 to 20 times the blade frequency at the impeller inlet as shown in Figure 26; these pressure pulsation amplitudes are small. The pitch motion affects the magnitude of the maximum pulsation amplitude. This amplitude gradually increases as the pitch period shortens and reaches a maximum value under a pitch period of 5 s.
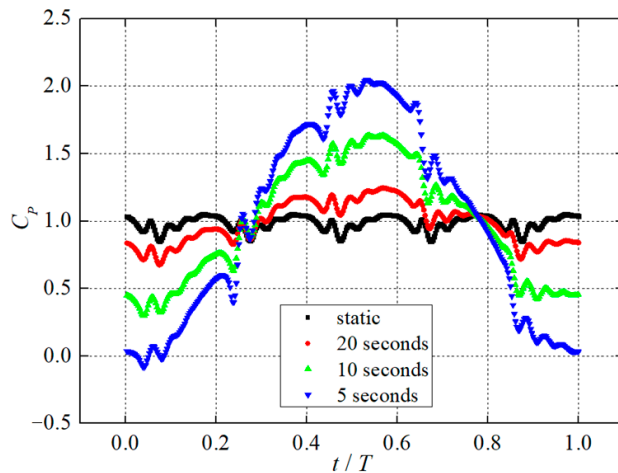

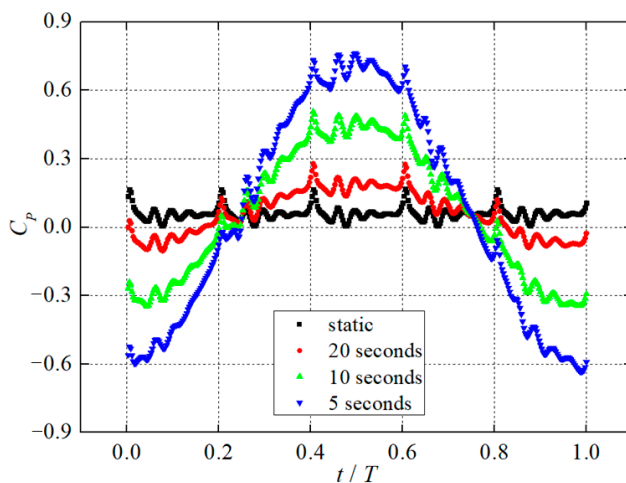**Figure 24.** Pressure variations with time at impeller inlet.

Figure 25. Pressure variations with time at impeller outlet.
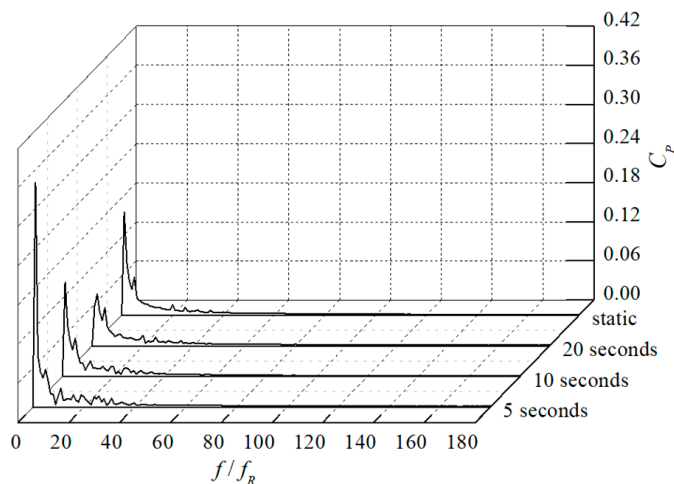

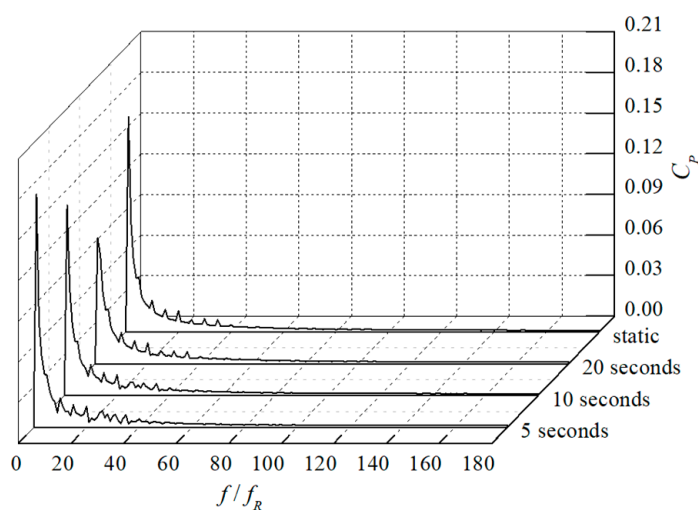**Figure 26.** Pressure variations in frequency domain at impeller inlet.

Figure 27. Pressure variations in frequency domain at impeller outlet.

4. Conclusions

This work investigates the effects of pitch motion on the performances and inner flow characteristics of a centrifugal pump. A hydraulic test platform with swing motion is established to analyze the pump performance variations between the static state and under the influence of pitch motion. A large eddy simulation with a shear-modified eddy viscosity model is employed to simulate inner flow excitation features under the influence of pitch motion based on a multiple-reference coordinate system. The research results are as follows:

(1) The head characteristic curve has an obvious hump zone under the low-flow-rate condition due to pitch motion. The hump curve generates pulsating variations in the pump flow rate and then produces some instability flows and flow excitation. The head gradually increases as the maximum pitch angle increases or the pitch period shortens. Under the rated flow conditions, the head decreases by 6.3% to reach a minimum at a maximum pitch angle of 20 degrees and a pitch period of 5 s;

(2) Some unsteady flows occur in the blade passage under the influence of pitch motion. Pitch motion mostly affects the flow structure in the blade inlet, where a slope velocity distribution and big velocity gradient exist. A distinct vortex flow appears near the blade suction surface and becomes increasingly turbulent as the pitch period shortens. Pitch motion provides an additional force to the centrifugal force and intensifies the unsteady stretching and deformation of the vortices;

(3) The pressure distribution presents an opposite slope at the blade outlet under the influence of pitch motion, compared with the static state. The time-domain variation in pressure mainly depends on the blade characteristics. A parabolic feature is present in the pressure curve under the influence of pitch motion, and the parabola's amplitude gradually increases as the pitch period shortens. The pitch motion affects the magnitude of maximum pressure pulsation amplitude in the frequency domain, and the amplitude reaches a maximum value under a pitch period of 5 s;

(4) This work provides some evidence in analyzing the effects of pitch motion on the operation characteristics of a ship pump. Future work will be conducted to explore pump operating characteristics under rolling conditions in comparison with those under the influence of pitch motion.

Author Contributions: Data curation, Y.Y.; Funding acquisition, Y.Y.; Investigation, W.G. and G.W.; Methodology, J.W.; Project administration, Y.Y.; Writing—original draft, Y.Y. All authors have read and agreed to the published version of the manuscript.

Data Availability Statement: No applicable.

Conflicts of Interest: The authors declare no conflict of interest.

References

1. Ghamkhar, K.; Ebrahimi, A.; Shariloo, K. Wavelet analysis of the flow field around an oscillating airfoil undergoing pure pitching motion at low Reynolds number. *Phys. Fluids* **2023**, *35*, 063607. [CrossRef]
2. Xu, B.; Kang, H.; Shen, X.; Li, Z.; Cai, X.; Hu, Z. Aerodynamic analysis of a downwind offshore floating wind turbine with rotor uptilt angles in platform pitching motion. *Ocean Eng.* **2023**, *281*, 114951. [CrossRef]
3. Guo, Y.; Wang, X.; Mei, Y.; Ye, Z.; Guo, X. Effect of coupled platform pitch-surge motions on the aerodynamic characters of a horizontal floating offshore wind turbine. *Renew. Energy* **2022**, *196*, 278–297. [CrossRef]
4. Chang, S.W.; Chen, Z.C. Hydrothermal performance of turbulent channel flow enhanced by spirally finned tube bundle in pitching and rolling motions. *Therm. Sci. Eng. Prog.* **2023**, *37*, 101567. [CrossRef]
5. Yan, B.H. Review of the nuclear reactor thermal hydraulic research in ocean motions. *Nucl. Eng. Des.* **2017**, *313*, 370–385. [CrossRef]
6. Hwang, J.; Lee, Y. Characteristics of critical heat flux under rolling condition for flow boiling in vertical tube. *Nucl. Eng. Des.* **2012**, *252*, 153–162. [CrossRef]
7. Jin, G.; Yan, C.; Sun, L.; Xing, D. Effect of rolling motion on transient flow resistance of two-phase flow in a narrow rectangular duct. *Ann. Nucl. Energy* **2014**, *64*, 135–143. [CrossRef]
8. Wang, Z.; He, Y.; Duan, Z.; Huang, C.; Yuan, Y.; Li, M.; Liu, S. Effects of rolling motion on transient flow behaviors of gas-liquid two-phase flow in horizontal pipes. *Ocean Eng.* **2022**, *255*, 111482. [CrossRef]
9. Tan, S.; Wang, Z.; Wang, C.; Lan, S. Flow fluctuations and flow friction characteristics of vertical narrow rectangular channel under rolling motion conditions. *Exp. Therm. Fluid Sci.* **2013**, *50*, 69–78. [CrossRef]
10. Abdelsalam, S.I.; Alsharif, A.M.; Elmaboud, Y.A.; Abdellateef, A.I. Assorted kerosene-based nanofluid across a dual-zone vertical annulus with electroosmosis. *Heliyon* **2023**, *5*, e15916. [CrossRef]
11. Chen, C.; Gao, P.; Tan, S.; Huang, D.; Yu, Z. Effect of rolling motion on two-phase frictional pressure drop of boiling flows in a rectangular narrow channel. *Ann. Nucl. Energy* **2015**, *83*, 125–136. [CrossRef]
12. Yuan, Y.; Fang, Y.; Tang, L. Effects of non-uniform elbow inflow on the unsteady flow and energy development characteristics of a centrifugal pump. *Phys. Fluids* **2023**, *35*, 015152. [CrossRef]
13. Yuan, Y.; Yuan, S.; Tang, L. Investigation on the effect of complex impeller on vibration characteristics for a high-speed centrifugal pump. *Proc. Inst. Mech. Eng. Part A J. Power Energy* **2020**, *234*, 611–624. [CrossRef]
14. Tang, L.; Yuan, S.; Tang, Y.; Qiu, Z. Optimization of impulse water turbine based on GA-BP neural network arithmetic. *J. Mech. Sci. Technol.* **2019**, *33*, 241–253. [CrossRef]
15. Zhu, Z.; Liu, H. Dynamic Pressure Test and Analysis of Marine Ballasted Centrifugal Pump under Rapid Changing Conditions. *J. Mar. Sci. Eng.* **2021**, *9*, 1299. [CrossRef]
16. Zhang, H.; Kong, F.; Zhu, A.; Zhao, F.; Xu, Z. Effect of Blade Outlet Angle on Acoustics of Marine Centrifugal Pump. *Acoust. Aust.* **2020**, *48*, 419–430. [CrossRef]
17. Abdelsalam, S.I.; Magesh, A.; Tamizharasi, P.; Zaher, A.Z. Versatile response of a Sutterbynanofluid under activationenergy: Hyperthermia therapy. *Int. J. Numer. Heat Fluid Flow* **2023**, *7*, 0961–5539.
18. Ye, C.; Tang, Y.; An, D.; Wang, F.; Zheng, Y.; van Esch, B.P.M. Investigation on stall characteristics of marine centrifugal pump considering transition effect. *Ocean Eng.* **2023**, *280*, 114823. [CrossRef]
19. Alawadhi, K.; Alzuwayer, B.; Alrahmani, M.; Murad, A. Evaluation of the Erosion Characteristics for a Marine Pump Using 3D RANS Simulations. *Appl. Sci.* **2021**, *11*, 7364. [CrossRef]
20. Xing, D.; Yan, C.; Sun, L.; Wang, C. Effect of rolling motion on single-phase laminar flow resistance of forced circulation with different pump head. *Ann. Nucl. Energy* **2013**, *54*, 141–148. [CrossRef]
21. Abdelsalam, S.I.; Bhatti, M.M. Unraveling the nature of nano-diamonds and silica in a catheterized tapered artery: Highlights into hydrophilic traits. *Sci. Rep.* **2023**, *13*, 5684. [CrossRef]
22. Xiao, H.L.; Luo, J.S. Shear-modified sub-grid model and its applications to turbulent channel flow. *J. Aerosp. Power* **2010**, *25*, 123–128.
23. Shim, H.S.; Kim, K.Y. Effects of the number of blades on impeller-volute interaction and flow instability of a centrifugal pump. *Proc. Inst. Mech. Eng. Part A J. Power Energy* **2022**, *236*, 1500–1517. [CrossRef]
24. Liu, Y.; Tan, L. Tip clearance on pressure fluctuation intensity and vortex characteristic of a mixed flow pump as turbine at pump mode. *Renew. Energy* **2018**, *129*, 606–615. [CrossRef]
25. Meng, Q.; Shen, X.; Zhao, X.; Yang, G.; Zhang, D. Numerical Investigation on Cavitation Vortex Dynamics of a Centrifugal Pump Based on Vorticity Transport Method. *J. Mar. Sci. Eng.* **2023**, *11*, 1424. [CrossRef]
26. Silveira, N.; Meghoe, A.; Tinga, T. Integration of multiple failure mechanisms in a life assessment method for centrifugal pump impellers. *Adv. Mech. Eng.* **2023**, *15*, 16878132231175755. [CrossRef]

27. Oro, J.M.F.; Perotti, R.B.; Vega, M.G.; González, J. Effect of the radial gap size on the deterministic flow in a centrifugal pump due to impeller-tongue interactions. *Energy* **2023**, *278 Pt A*, 127820.

28. Capurso, T.; Bergamini, L.; Torresi, M. Performance analysis of double suction centrifugal pumps with a novel impeller configuration. *Energy Convers. Manag. X* **2022**, *14*, 100227. [CrossRef]